Weierstraß-Institut

für Angewandte Analysis und Stochastik

Leibniz-Institut im Forschungsverbund Berlin e. V.

Preprint ISSN 2198-5855

Modeling and efficient simulations of broad-area edge-emitting semiconductor lasers and amplifiers

Mindaugas Radziunas

submitted: 5 September 2016

Weierstrass Institute
Mohrenstr. 39
10117 Berlin
Germany
E-Mail: mindaugas.radziunas@wias-berlin.de

No. 2292
Berlin 2016

2010 *Mathematics Subject Classification.* 35Q60 65Y05 68W10 68W15 78-04.

Key words and phrases. Traveling wave model, numerical scheme, simulations, parallel computations, MPI, semiconductor device, broad area.

This work was supported by the Einstein Center for Mathematics Berlin under project D-OT2.

Edited by
Weierstraß-Institut für Angewandte Analysis und Stochastik (WIAS)
Leibniz-Institut im Forschungsverbund Berlin e. V.
Mohrenstraße 39
10117 Berlin
Germany

Fax: +49 30 20372-303
E-Mail: preprint@wias-berlin.de
World Wide Web: http://www.wias-berlin.de/

ABSTRACT. We present a (2+1)-dimensional partial differential equation model for spatial-lateral dynamics of edge-emitting broad-area semiconductor devices and several extensions of this model describing different physical effects. MPI-based parallelization of the resulting middle-size numerical problem is implemented and tested on the blade cluster and separate multi-core computers at the Weierstrass Institute in Berlin. It was found, that an application of 25-30 parallel processes on all considered platforms was guaranteeing a nearly optimal performance of the algorithm with the speedup around 20-25 and the efficiency of 0.7-0.8. It was also shown, that a simultaneous usage of several in-house available multi-core computers allows a further increase of the speedup without a significant loss of the efficiency. Finally, an importance of the considered problem and the efficient numerical simulations of this problem were illustrated by a few examples occurring in real world applications.

1. INTRODUCTION

High power high brightness edge-emitting broad-area semiconductor (BAS) lasers and optical amplifiers are compact, efficient and reliable light sources playing a crucial role in different laser technologies, such as free space communications [1], three-dimensional printing, marking, materials processing [2], pumping fiber amplifiers [3], or optical frequency conversion [4]. BAS lasers and amplifiers have a relatively simple geometry [see Fig. 1(a)] allowing an efficient current injection through a broad electric contact on the top of the device and can operate at high power (tens of Watts) regimes.

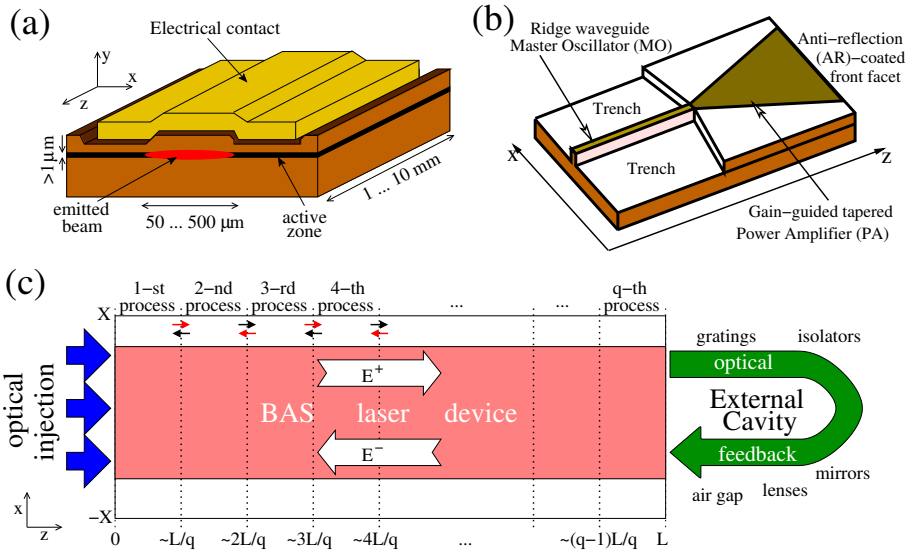

FIGURE 1. Schematic representations of edge-emitting semiconductor laser devices. (a): BAS device with a single broad electrical contact. (b): Master Oscillator – tapered Power Amplifier (MOPA) device. (c): Simplified representation of the BAS device, as considered in the (2+1)-dimensional TW model. Thin vertical dotted lines indicate decomposition of the computational domain to several sub-domains, each treated by a separate process. Small red and black arrows represent localized data exchange between adjacent processes redfollowing red-black parallel data communication algorithm.

However, BAS devices have one serious drawback: operated at high power, they suffer from a low beam quality due to simultaneous irregular contributions of different lateral and longitudinal optical modes. As a result, the emitted optical beam is irregular, has undesirable broad optical spectra, and large divergence [5]. Thus, a quality improvement of the beam amplified in BAS amplifiers or generated by BAS lasers is a critical issue of the modern semiconductor laser technology.

Many laser design concepts are used to achieve an improvement of the beam quality, each of them, however, having their drawbacks. For example, a Master Oscillator (MO) – Power Amplifier (PA) laser shown in Fig. 1(b) consists of the narrow waveguiding MO part generating a stable stationary optical field which later is amplified in the tapered PA part of the device. It should be noted, however, that the energy conversion efficiency of this device usually does not exceed 50-55% [6], and the residual field reflectivity at the PA facet can lead to undesired instabilities induced by the nonlinear interaction of multiple *longitudinal* modes [7, 8]. Thus, modeling, simulations and analysis of various high-power edge-emitting BAS devices are still strongly required.

The dynamics of BAS devices can be described in different ways. The most comprehensive approach resolving the spatiotemporal evolution of full semiconductor equations self-consistently coupled to the optical fields is given by 3 (space) +1 (time)-dimensional nonlinear PDEs [9]. Such model can be used for investigation of the static characteristics of the semiconductor lasers, but, due to the required long transient simulations, is inefficient for the study of the laser dynamics or laser operation dependence on the model parameters.

Since the *height* of the active zone where the optical beam is generated and amplified (y dimension) is considerably smaller than the longitudinal (z) and lateral (x) dimensions of a typical BAS device [see Fig. 1(a)], a significant simplification can be achieved by averaging over the vertical direction and by describing certain effects phenomenologically. The resulting (2+1)-dimensional dynamical traveling wave (TW) model [10, 11, 12, 7] can be resolved numerically orders of magnitudes faster allowing for parameter studies in an acceptable time. Individual laser devices admit further model reductions implying systems of (1+1)-dimensional PDEs [13, 14], DDEs [15], or ODEs [14], which still can recover the major dynamical effects in the considered BAS devices.

Seeking to understand dynamics of BAS devices, to suggest improvements to existing devices or to propose novel device design concepts, we do a variety of related tasks. Namely, we perform modeling at different levels of complexity [7, 13, 15, 14], do a mathematical analysis of the hierarchy of models, create and implement efficient and robust numerical algorithms [16, 17, 18], and make numerical integration of the model equations [19]. Typically, all these steps are done within research projects in cooperation with developers of the devices.

In this paper, we present the basic (2+1)-dimensional TW model and its several extensions describing material gain dispersion, optical feedback from various external cavities, and different thermal effects. For the numerical integration of our most complex model, we use a split-step Fourier method based numerical algorithm [18]. Since the optimization simulations of the laser devices require huge CPU time and memory resources, we have parallelized our algorithm and implemented it on different multi-core compute servers at the Weierstrass Institute in Berlin [18, 19]. A presented parameter optimization simulation example has shown that due to this implementation, typical one-parameter studies requiring a few month single-process simulations can be efficiently performed during a few days.

The main aim of this paper is testing the performance of our parallel algorithm on different in-house available compute servers. For given middle-size problems, the acceptable speedup factor of 20-25 can be already achieved by exploiting 25-30 parallel processes which can be executed on the single available multi-core computer. We have also shown that a larger speedup with a similar efficiency can be achieved by simultaneous exploitation of two or even more multi-core computers. Some results on the performance of the parallel algorithm executed on the (rather old) blade cluster "euler" at the Weierstrass Institute in Berlin were presented in the conference proceedings paper [20]. In the present paper, we provide additional details on the blade cluster performance as well as test and analyze the performance of a single and several in-house available newer multi-core compute servers. Modeling and simulation of thermal lensing impact on the angular shape of the radiated optical field were also presented for the first time in this paper.

2. Mathematical modeling

The simplest version of the TW model is a degenerate system of second order PDEs for the slowly varying complex amplitudes of the counter-propagating optical fields, $E(z,x,t) = (E^+, E^-)^T$ [see white arrows in Fig. 1(c)], nonlinearly coupled to a rate equation for the real carrier density distribution $N(z,x,t)$. It accounts for the diffraction of the fields and diffusion of the carriers in the lateral direction, whereas spatially non-homogeneous device parameters capture the geometrical design of the device. The TW model reads as

$$
\begin{aligned}
\tfrac{n_g}{c_0}\tfrac{\partial}{\partial t}E &= \left[\left(\begin{smallmatrix}-1 & 0\\ 0 & 1\end{smallmatrix}\right)\tfrac{\partial}{\partial z} - \tfrac{i}{2\bar{n}k_0}\tfrac{\partial^2}{\partial x^2}\right]E \\
&\quad + \left[\mathcal{B}(N,\|E\|^2) - (\alpha + i\delta)\,\mathcal{I}\right]E + F_{sp}, \\
\tfrac{\partial}{\partial t}N &= D\tfrac{\partial^2}{\partial x^2}N + I(z,x) - (AN + BN^2 + CN^3) \\
&\quad - \tfrac{2c_0}{n_g}\Re\left[E^{*T}\mathcal{B}(N,\|E^{\pm}\|^2)E\right],
\end{aligned}
\tag{1}
$$

where $\mathcal{I}$ is the 2×2-dimensional identity matrix, c_0, k_0, n_g, $\bar{n}$, α, δ, D, I, A, B, and C represent the speed of light in vacuum, the central wavenumber related to the central wavelength $\lambda_0 = \frac{2\pi}{k_0}$, the group velocity index in the semiconductor material, the background refractive index, the field losses, the built-in contrast of the refractive index, the carrier diffusion, the injected current density, and three spontaneous carrier recombination parameters, respectively. The 2×2-dimensional complex matrix $\mathcal{B}$ models the carrier and photon density dependent semiconductor material gain, $G(N,\|E^{\pm}\|^2)$, the carrier-induced changes of the refractive index, $\tilde{n}(N)$, as well as the distributed coupling of the counter-propagating fields, κ:

$$
\begin{aligned}
\mathcal{B}_{11} &= \mathcal{B}_{22} = \tfrac{G(N,\|E\|^2)}{2} + i\tilde{n}(N), \\
\mathcal{B}_{12} &= \mathcal{B}_{21} = -i\kappa,
\end{aligned}
\tag{2}
$$

where $\kappa \in \mathbb{R}$. The gain and refractive index functions depend on the properties of semiconductor material and the design of the device, and in general, should be adjusted individually for each considered laser. A satisfactory description of these functions for a broad class of semiconductor lasers is given by the logarithmic and the square-root like expressions [7]

$$
G(N,\|E\|^2) = \tfrac{g'\log(\max(N,N_*))}{1+\varepsilon\|E\|^2},\ \ \tilde{n}(N) = \sigma\sqrt{N},
\tag{3}
$$

where g', σ, ε, and N_* are the differential gain, the refractive index scaling, the nonlinear gain compression, and the small carrier density used to determine an appropriate cut-off of the logarithmic gain function. Finally, the spontaneous emission factor F_{sp} in (1) denotes stochastic Langevin forces realized by appropriately using the random number generator [7]. We note, however, that for well-biased lasers considered in this paper, the spontaneous emission plays only a minor role causing only small perturbations of deterministic dynamic regimes.

In general, this model should be considered in the (laterally) unbounded region $Q = Q_{z,x} \times (0,T]$, where $Q_{z,x} = \{(z,x) : \ (z,x) \in (0,L) \times \mathbb{R}\}$ is the spatial domain, L represents the length of the device, x is the coordinate of the unbounded lateral axis of the device, and T defines the length of the time interval where we perform the integration. Far from the active zone, the optical fields and carriers usually are well damped. Thus, in our numerical simulations, we truncate the lateral domain at $x = -X$ and $x = X$ so that the truncated domain $Q^t_{z,x} = \{(z,x) : \ (z,x) \in (0,L) \times [-X,X]\}$ [large rectangular in Fig. 1(c)] contains the considered BAS device [pink area in the same figure]. Next, we assume either periodic boundary conditions [18, 16] or mixed Dirichlet (for the carrier densities) / approximate transparent (for the field functions) boundary conditions [17].

The boundary conditions for the optical fields at the longitudinal edges of the device, $z = 0$ and $z = L$, account for reflections of the counter-propagating fields and optional injection of external optical beams, $a_0(x,t)$ and $a_L(x,t)$:

$$\begin{aligned} E^+(0,x,t) &= r_0 E^-(0,x,t) + a_0(x,t), \\ E^-(L,x,t) &= r_L E^+(L,x,t) + a_L(x,t), \end{aligned} \tag{4}$$

with r_0 and r_L denoting the complex field reflectivity parameters at the laser facets.

The basic TW model described above can be reduced to lower dimensional systems, allowing a more detailed analysis, understanding, and control of specific dynamical effects [14, 13, 15]. On the other hand, different extensions of the basic TW model allow achieving a more precise description of various relevant properties of BAS devices.

2.1. **Gain dispersion.** First of all, an introduction of a couple of linear equations for induced polarization functions $P^+(z,x,t)$ and $P^-(z,x,t)$ enables modeling of nontrivial material gain dependence on the lasing frequency [21]:

$$\begin{aligned} &\mathcal{B}_{\text{new}} = \mathcal{B} - \mathcal{I}\mathcal{D}, \qquad \mathcal{D}E^\pm := \overline{g}\,(E^\pm - P^\pm)\,, \\ &\tfrac{\partial}{\partial t} P^\pm = i\overline{\omega} P^\pm + \overline{\gamma}\,(E^\pm - P^\pm)\,. \end{aligned} \tag{5}$$

Here, the parameters $\overline{g}$, $\overline{\omega}$, and $\overline{\gamma}$ define the Lorentzian fit of the gain profile and denote the amplitude, the central frequency, and the half width at half maximum of this Lorentzian, respectively. The introduction of Eqs. (5) implies an efficient optical frequency selection mechanism and ensures a smoothening effect on the solution of the system (1)-(4).

2.2. **Optical feedback.** A useful extension of the basic TW model equations can be provided by the model of the optical feedback which should be taken into account when considering diode lasers with different external cavities (ECs). In the presence of the optical feedback from the EC [thick green arrow in Fig. 1(c)], the optical injection function $a_L(x,t)$ in Eq. (4) should be replaced by the corresponding (delayed) feedback term. This term can be obtained by resolving the linear wave equations in the air and accounting for various field transmission/reflection relations within the different components (lenses, gratings, apertures, etc.) of the EC.

For example, in the case of a simple EC composed of the collimating lens and the flat mirror located perpendicularly to the optical axis of the BAS device, the re-injection term can be given by a simple delay term

$$a_L = t_L^2 \sqrt{R_{ec}}\, e^{i\varphi_{ec}} E^+ \left(L, x, t - \tau_{ec}\right).$$

Here, $t_L = \sqrt{1 - |r_L|^2}$ is the field amplitude transmission through the right facet of the laser, R_{ec} and φ_{ec} are the field intensity reflection and phase change in the EC. $\tau_{ec} = 2d_{ec}/c_0$ is the field propagation time in the external cavity. It is determined by the field velocity in vacuum c_0 and the distance d_{ec} from the center of the right facet of the BAS diode to the external reflector (which, in this case, coincides with the distance between the facet and the external mirror). When the collimating lens is absent, and the reflector or the diffractive grating is located at the small angle α_{EC} to the optical axis, the feedback term turns to be more complicated [22]:

$$a_L \approx t_L^2 \sqrt{\tfrac{-i}{2d_{ec}\lambda_0}}\, \mathcal{F} \int\limits_{x' \in \mathbb{R}} E^+(L, x', t - \tau_{ec}) e^{-ik_0 \rho(x,x')} dx'.$$

Here, $\rho(x, x')$ is the *shortest* distance between two lateral points x' and x at the diode facet that the light takes to travel via the (infinitely broad) external reflector, whereas the operator $\mathcal{F}$ accounts for the spectral filtering by the external grating.

The feedback term of another EC including the lens, the refractive grating located at the angle α_{ec} to the optical axis, and the small reflecting aperture [23] can be written as

$$a_L \approx \tfrac{-r_g^2 T_L^2}{2\pi} \int_{\mathbb{R}} e^{i\omega(t - 8f/c_0)} \chi\left(\tfrac{\lambda_0 f \cot\alpha_{ec}}{2\pi c_0}\omega - x\right) \times \\ \times \int_{\mathbb{R}} e^{-i\omega t'} E^+(L, x, t') dt'\, d\omega.$$

Here, ω denotes the relative optical frequency of the field, f is the focal distance of the lense, r_g and $\chi(x)$ are the field amplitude reflections at the grating and aperture (the step-function $\chi(x)$ is non-vanishing and takes the value of 1 if only x belongs to the aperture).

2.3. **Thermal effects.** In many cases, a theoretical reproduction of experimental observations of high-power BAS devices requires an appropriate treatment of the thermal effects. Proper self-consistent coupling and numerical resolution of the TW and the heat transport models are very challenging tasks, since, in general, one should account for all three spatial coordinates of the device as well as for different time scales ranging from picoseconds (photon lifetime) to microseconds (thermal diffusion).

Slow changes in the temperature distribution $\theta(z, x, t)$ within BAS devices admit a rather easy method for the qualitative modeling of the thermal effects. For example, a well-known heating-induced effect in semiconductor lasers is a red shift of the operating wavelength with an increasing heating of the device. Theoretically, such a wavelength shift can be realized by uniform changes of the detuning factor δ entering the TW model equations (1). More complicated wavelength shifting and jumping scenarios are reported in semiconductor lasers with several separate electrical contacts [7, 8, 13, 21]. In Refs. [7, 13], we have proposed to model a bias current induced (Joule) heating effects by the following modification of the detuning factor δ:

$$\delta_{\text{new}}(z, x) = \delta(z, x) + \iint c_T(z, x, \tilde{z}, \tilde{x}) I(\tilde{z}, \tilde{x}) d\tilde{z} d\tilde{x}. \tag{6}$$

The inclusion of the linear nonlocal refractive index dependence on the inhomogeneous injection $I(x, z)$ is realized by a non-vanishing peace-wise constant function c_T describing local and nonlocal crosstalk thermal effects in BAS devices with a single or several electrical contacts. This simple model with the properly defined [13] contact-wise constant coefficient c_T allows

a proper theoretical reproduction of the state jumping behavior with the tuning of the injected currents [7]. Similarly one can model the Joule heating induced shift of the gain peak frequency $\overline{\omega}$:

$$\overline{\omega}_{\text{new}}(z,x) = \overline{\omega}(z,x) + \iint \nu_T(z,x,\tilde{z},\tilde{x}) I(\tilde{z},\tilde{x}) d\tilde{z} d\tilde{x},$$

where ν_T is the contact-wise constant function determined by several non-vanishing constants[7].

We note, however, that the parametric Joule heat modeling discussed above is not sufficient for a correct reproduction of the experimentally measured thermal effects on the lateral and angular shape of the optical beams in high-power BAS devices. Namely, the lateral heat distribution implies a corresponding distribution of the refractive index, which, in turn, acts as a lens, imposing narrowing of the optical field within the BAS device and corresponding broadening of the radiation angle [12]. In order to include the effects of thermal lensing, we allow a spatial distribution of the refractive index detuning factor

$$\delta_{\text{new}}(z,x) = \delta(z,x) + c_\theta \theta(x), \tag{7}$$

where the thermal lensing function $c_\theta \theta(x)$ should be estimated experimentally or precomputed using the heat transport model defined within the transversal crossection of the semiconductor device [24].

3. Numerical algorithm and its parallelization

For the numerical integration of the (2+1)-dimensional TW model, we use either a full finite difference (FD) scheme (implemented and tested on the parallel computer cluster at the TU Vilnius, Lithuania) [16, 17] or a split-step fast Fourier transform (SS-FFT) based numerical method (implemented and used at different computer servers at the Weierstrass Institute in Berlin) [7, 18].

For the approximation of the field equations in (1), we exploit a spatial-temporal mesh, which is uniform in z and t directions and can be weakly nonuniform in a lateral x direction in the FD approach case. In both cases, the group velocity defines the fixed ratio of the longitudinal (h_z) and temporal (h_t) steps of the mesh: $\frac{c_0}{n_g} = \frac{h_z}{h_t}$. Thus, the diagonals of the mesh in the z-t plane coincide with the characteristic directions $z \pm \frac{c_0}{n_g} t = \text{const}$ of the field equations in (1). The carrier rate equations in (1) are approximated on the staggered grid in the FD approach case[17] or on the same grid in the SS-FFT approach case[18].

Typically, $\bar{\gamma}$ in polarization equations (5) is large and, therefore, these equations are stiff. To resolve them numerically, we use an exponentially weighted scheme, which ensures, that in the limit $\bar{\gamma} \to \infty$ the discretized solutions $P^{\pm}$ converge to $E^{\pm}$[17, 18].

The main difference of the FD and SS-FFT approaches is the method how the lateral field diffraction and carrier diffusion (determined by the operator ∂_x^2) is taken into account during each time iteration step. In the FD approach, these operators are approximated by the Crank-Nicolson-type finite differences, whereas the resulting implicit schemes in the lateral direction are efficiently resolved by the standard factorization method. In the SS-FFT approach, these operators are separately resolved in the Fourier domain using the discrete FFT algorithm.

We also note that the SS-FFT approach, which is fast, robust, and reliable method widely used in nonlinear optics and optoelectronics, relies on the periodic lateral boundary conditions for E and N and laterally-constant field diffraction and carrier diffusion coefficients. In contrast, the FD approach allows different types of lateral boundary conditions (including transparent

boundary conditions[17]) and laterally varying carrier diffusion and field diffraction factors. Full formulations of the FD and SS-FFT numerical schemes can be found in Ref. [17] and Ref. [18], respectively.

Precise dynamic simulations of long and broad devices and tuning/optimization of the model parameters require huge process time and memory resources. A proper resolution of rapidly oscillating fields in typical BAS devices in a sufficiently large optical frequency range requires a fine space ($10^6 - 10^7$ mesh points) and time (up to 10^6 points for typical 5 ns transients) discretization. Without a parallelization of the algorithm, dynamic simulations of such devices can easily take several days or even weeks. Some speedup of computations can be achieved by using problem-dependent variable grid steps [17]. However, for extended parameter studies with the numerical integration times up to 1000 ns parallel computers and parallel solvers have to be employed.

The method of the domain decomposition and MPI libraries are used to parallelize the sequential algorithm. Namely, the numerical mesh of the full problem defined by N_z longitudinal and N_x lateral uniform discretization steps is split along the longitudinal z-direction into q (q: number of processes) non-overlapping rectangular sub-grids of the similar size $(N_{z,j} \times N_x)$, $j = 1, \ldots, q$, $N_{z,j} \approx N_z/q$. Such one-dimensional domain decomposition allows avoiding additional complications when resolving lateral field diffraction and carrier diffusion using the FFT (in the SS-FFT based numerical scheme) or the factorization algorithm (in the FD approach).

Below in this paper, we analyze the performance of the SS-FFT based parallel numerical algorithm used on different computers at the Weierstrass Institute in Berlin. Before execution of each time iteration step, any two adjacent sub-domain processes need to exchange a local information on the $7N_x$ real numbers representing complex field functions E^+ and E^-, a complex polarization function P^+ or P^-, and a real function N at the both sides of the sub-domain interface [18]. A schematic representation of the domain decomposition is also shown by thin vertical dotted lines in Fig. 1(c). The data exchange by adjacent processes is realized according to the well-known non-blocking red-black parallel data communication algorithm. Namely, the (red) processes attributed to the subdomains with odd indices choose to send while (black) processes operating at the subdomains with even indices receive, followed by a reversal of roles. Such consequent communications are schematically indicated by the small red and black arrows in Fig. 1(c), respectively.

The computational and the data exchange costs of each process involved in our parallel calculations for a single time iteration step can be approximated by

$$T_{\mathsf{c}}^{(q)} \leq c_1 \left\lceil \frac{N_z}{q} \right\rceil N_x \log N_x, \quad T_{\mathsf{e}}^{(q)} \leq c_2 \left(\alpha_{\mathsf{e}} + \beta_{\mathsf{e}} N_x\right). \tag{8}$$

Here, the factor $N_x \log N_x$ is due to the FFT, α_{e} denotes the (maximal) message startup time, β_{e} is the time required for sending 7 real numbers to the neighboring process, whereas c_1 and c_2 are proportionality constants. The total complexity of the parallel algorithm is given by

$$T_{\mathsf{tot}}^{(q)} = c_1 \left\lceil \frac{N_z}{q} \right\rceil N_x \log N_x + c_2 \left(\alpha_{\mathsf{e}} + \beta_{\mathsf{e}} N_x\right).$$

Thus, under the ideal conditions (identical and equally loaded processes, no extra waiting time before starting the next time iteration), the efficiency factor $\mathcal{E}^{(q)}$ of our computations can be written as

$$\mathcal{E}^{(q)} = \frac{t_{\mathsf{it}}^{(1)}}{q t_{\mathsf{it}}^{(q)}} \approx \frac{T_{\mathsf{c}}^{(1)}}{q T_{\mathsf{tot}}^{(q)}} \approx 1 - \mu q, \quad \mu = \frac{c_2(\alpha_{\mathsf{e}} + \beta_{\mathsf{e}} N_x)}{c_1 N_z N_x \log N_x}. \tag{9}$$

Here, μq is small, q is the number of applied parallel processes, $t_{\text{it}}^{(q)}$ denotes the time required for the integration of the problem on these q processes, whereas $t_{\text{it}}^{(1)}$ is the reference time, needed for the calculation of the same problem using a single process. The below-considered speedup factor of parallel calculations is given by $\mathcal{S}^{(q)} = q\mathcal{E}^{(q)}$.

4. PERFORMANCE OF THE ALGORITHM

Below in this section, we discuss the performance of the parallel numerical SS-FFT based algorithm[18] implemented at different servers available at the Weierstrass Institute in Berlin.

4.1. **Performance of the parallel cluster of computers.** First of all, our parallel algorithm was implemented on the WIAS blade cluster "euler" (Hewlett-Packard CP3000BL) consisting of 32 blades of the type HP BL460c. Each blade is equipped with two INTEL Xeon5430/2666 Quad Core processors and provides 16 GB of RAM. All nodes are interconnected via Infiniband 4xDDR (20 Gbit/s). This blade cluster was successfully used for simulations of nonlinear dynamics in BAS devices already since 2008, whereas the results of these simulations were reported in different engineering and applied physic conferences and journals, see, e.g., Refs.[7, 8, 12, 13, 14, 22]. The performance of the algorithm on this server was already briefly discussed in Refs.[18, 20].

To test the performance of this cluster, we have simulated three test problems, each of them defined on different spatial meshes having, however, the same amount of the mesh points. Namely, our test problems I, II, and III were determined on the meshes $(N_z \times N_x) = (320 \times 2048)$, (640×1024), and (1280×512), representing the computational domains $Q_{z,x}^t$ of the physical size (1.6 mm$\times 1024\,\mu$m), (3.2 mm$\times 512\,\mu$m), and (6.4 mm$\times 256\,\mu$m), respectively. The number of time iterations N_t in all cases was 272, corresponding to 16 ps long transients.

For characterization of the performance of the parallel computer cluster and our algorithm, we simulated the test problems using a different number of processes per each node of the cluster. The speedup $\mathcal{S}_q$ and the efficiency $\mathcal{E}_q$ of the parallel calculations of three test problems are shown in upper and lower diagrams of Fig. 2, respectively. In the ideal case, $\mathcal{S}_q = q$ and $\mathcal{E}_q = 1$ (see dashed lines in these diagrams). Due to the non-vanishing contribution of the data exchange cost between different processes ($T_{\text{e}}^{(q)} > 0$), however, both these factors are not reaching the ideal value.

According to Eqs. (8), both computational and data exchange costs, $T_{\text{c}}^{(q)}$ and $T_{\text{e}}^{(q)}$, are growing with the growth of the lateral mesh size N_x. Thus, the simulation time $t_{\text{it}}^{(q)}(k)$ needed to calculate three test problems with $k = I, II, III$, satisfies the relation

$$t_{\text{it}}^{(q)}(I) > t_{\text{it}}^{(q)}(II) > t_{\text{it}}^{(q)}(III),$$

see, e.g., Table 1, where calculation time $t_{\text{it}}^{(1)}$ of three test problems executed on different considered computers are given. The $\log N_x$ term in the expression of $T_{\text{c}}^{(q)}$ and the linear term $\beta_{\text{e}} N_x$ within $T_{\text{e}}^{(q)}$ suggest, however, a faster growth of the data exchange contribution and, therefore, a growth of the factor μ in Eq. (9) with the increasing N_x in the considered test problems. A corresponding increase of $\mathcal{E}^{(q)}$ with a decreasing N_x is confirmed in three lower panels of Fig. 2.

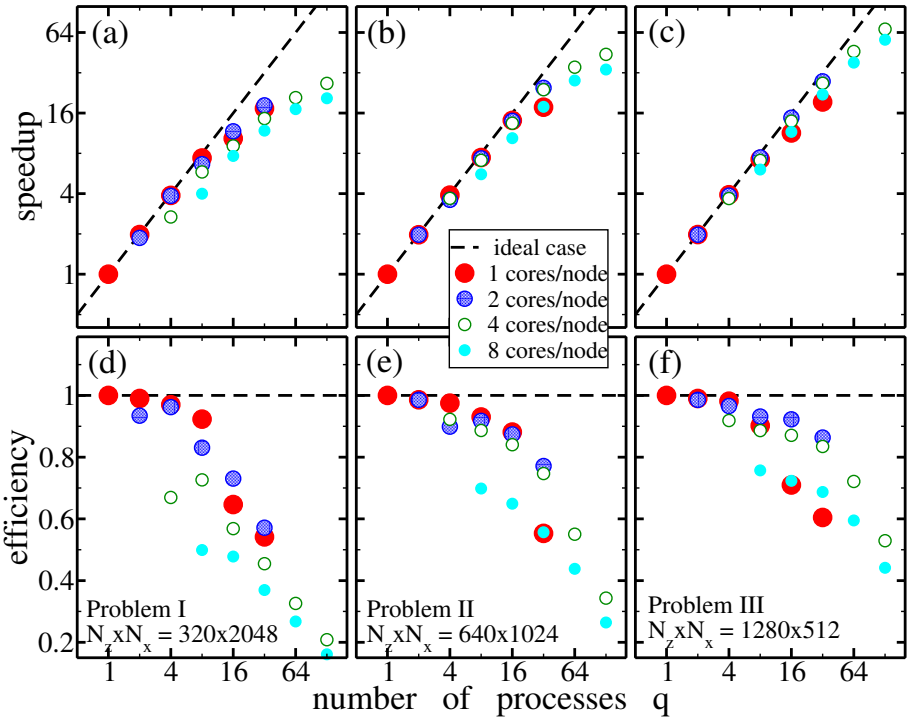

FIGURE 2. Speedup [(a), (b) and (c)] and efficiency [(d), (e) and (f)] of multi-process simulations on the blade cluster. Panels [(a), (d)], [(b), (e)], and [(c), (f)] represent simulations of test problems I, II, and III. Bullets of different color indicate tests with 1, 2, 4 or 8 cores used on each node, and a single process running on each core. Dashed lines indicate an ideal speedup (upper panels) and efficiency (lower panels), respectively.

The numerical test results presented in Fig. 2 show that for a different number of processes q, the best efficiency of numerical simulations was achieved when exploiting a single (full red bullets) or two (hatched blue bullets) cores per each node. For Problems II and III, a nearly optimal performance characterized by the speedup factor ~ 25 and efficiency ~ 0.8 could be found when performing 32-process calculations. In the case of Problem I, the application of 32 or more processes implies the dominance of the data exchange contribution $T_{\mathrm{e}}^{(q)}$ over the calculation costs $T_{\mathrm{c}}^{(q)}$, what degrades the calculation efficiency and saturates the growth of the speedup. More details on the performance and scalability of the parallel algorithm can be found in Ref.[18].

4.2. **Performance of the multi-core computers.** Due to the old age of the blade server “euler”, we have also implemented our parallel algorithm on much newer multi-core (MC) computers available at the Weierstrass Institute using open source MPI libraries (Open MPI, version 1.7.2).

Below in this section, we discuss the calculation experiments performed on HP BL460c Gen9 2xXeon Fourteen-Core 2600MHz with 256 GB RAM (“host 1”) and HP BL460c Gen9 Intel 2xXeon Sixteen-Core 2300 MHz with 512 GB RAM (“host 2”) compute servers.

First, we have performed calculations of the test problems exploiting multiple cores of the same host 1. The speedup and the efficiency of these calculations are represented by the red hatched

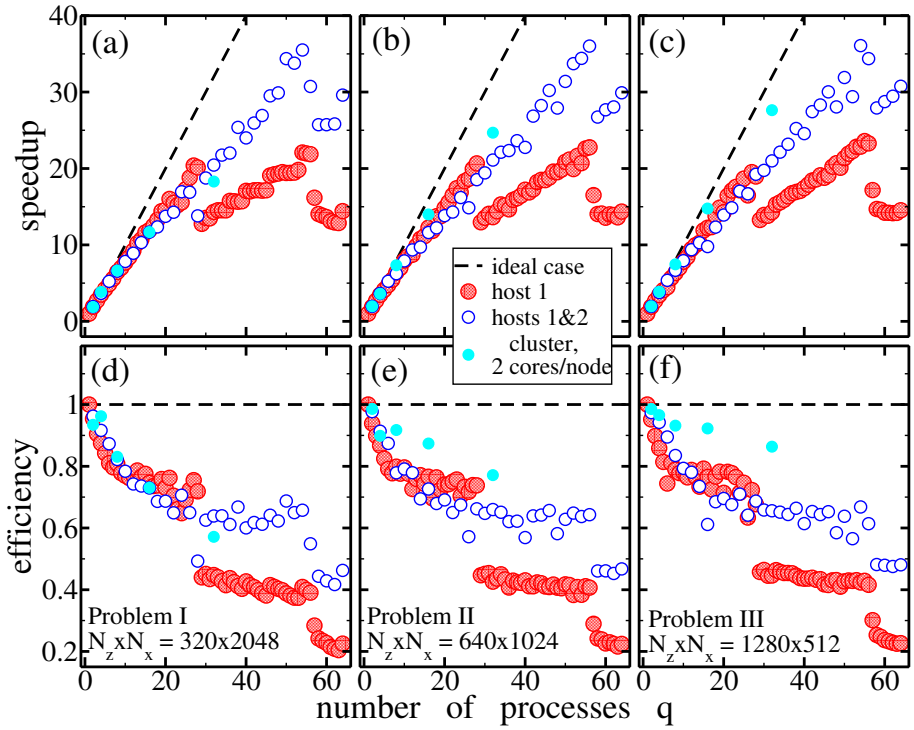

FIGURE 3. Speedup and efficiency of multi-process simulations for three test problems. Red shaded and empty blue bullets: simulations on the single and the both multi-core hosts, respectively. Full cyan bullets: simulations on the blade cluster exploiting two cores per node. The meaning of dashed lines, as well as all panels and meshes of the test problems, are as in Fig. 2.

bullets in Fig. 3. In all cases, once the number of processes per each of 28 cores of the host 1 was not larger than one, the efficiency $\mathcal{E}^{(q)}$ was remaining greater than 0.7. The biggest speedup achieved for $q = 28$ was around 20. For $q > 28$, at least one core was containing a couple of simultaneously executed processes. The efficiency was nearly halved in this case, and no further speedup of calculations was available. Another drop of the efficiency occurs when q exceeds 56, which is a total number of *logical* cores with hyperthreading enabled on the host 1. We admit that our earlier calculations on the computer cluster have allowed achieving better

TABLE 1. Calculation time of three test problems using single process on a single core belonging to three different computers.

	Problem I (320×2048)	Problem II (640×1024)	Problem III (1280×512)
Blade cluster	236.282 s	226.594 s	224.934 s
MC host 1	86.352 s	84.026 s	83.854 s
MC host 2	95.266 s	91.958 s	88.395 s

overall speedup and efficiency: see, e.g., full cyan bullets in Fig. 3, which represent already discussed simulations performed using two processes on each node of the cluster. On the other hand, the efficiency factor $\mathcal{E}^{(q)} \approx 0.7$ achievable when exploiting one process per each of all 28 cores of the host 1 (red bullets in the lower panels of Fig. 3 at $q = 28$) is similar or even better

compared to the case when all cores within the nodes of the blade cluster were exploited (cyan bullets in the lower panels of Fig. 2).

The performance of the single process calculations of the newer MC computers is nearly three times higher than those of the old blade cluster (see Table 1). We also note, that the largest speedup achieved by the whole blade cluster consisting of 32 nodes is around 60, see upper panels of Fig. 2. Thus, calculations with 28 processes and the speedup factor 20 on the host 1 can be performed almost at the same time as similar calculations on the whole blade cluster.

In the case, when the longitudinal grid size, N_z, is large, and the faster execution of the problems is required, one can also exploit other available MC computers. Blue empty bullets in Fig. 3 represent simulations of the test problems performed on both hosts 1 and 2. For the optimal performance, all processes were equally distributed between two hosts, and only a single process (if possible) was attributed to each core on these hosts. One can see, that up to $q = 56$, we could observe a monotonous growth of the speedup and only a slight decay of the efficiency. The maximal speedup in all three test problems was more than 35.

5. Applications: simulations of thermal effects

Simulations and analysis of the TW model (1)-(5) were extensively used for optimization of the existing devices and creation of the novel BAS device design concepts[7, 8, 13, 14, 22]. In this section, we present an application of our model, numerical algorithm, and software for the study of thermal effects in BAS devices. Here we exploit parametric dependences of the refractive index (detuning factor) on the Joule heating (6) and the spatial distribution of the temperature (7).

To illustrate a thermal detuning induced jumping between different operating states, we have considered a MOPA laser with a non-vanishing field coupling factor κ in the MO part of the device, see Fig. 1(b) for a schematic representation of the MOPA laser. The narrow waveguide of the distributed feedback (DFB) MO generates a stable optical beam determined by a single *transversal* optical mode, which later is amplified in the tapered PA part of the device. An ideal MOPA laser should be able to maintain a high quality of the emitted beam. The operation of realistic MOPA devices, however, is spoiled by the amplification of the spontaneous emission in the PA, by the small separation of the MO and PA electrical contacts, and by the residual field reflectivity at the PA facet of the device.

In Refs. [7, 13], we have analyzed how this residual reflectivity and thermally induced changes (6) of the refractive index imply experimentally observable unwanted switchings between operating states determined by adjacent *longitudinal* optical modes. We have found that these bifurcations are due to the changing phase relations of complex forward- and back-propagating fields at the interface of the MO and PA parts of the device. In the absence of the thermal detuning ($c_T \equiv 0$), the tuned injected current I in one of the laser parts implies only marginal changes of this phase relation. Consequently, the state jumps in the simulated MOPA devices are absent, what is in contrast to experimental observations.

After applying a correctly estimated thermal detuning ($c_T \neq 0$), we could simulate a typical experimentally observable state-jumping behavior with an increasing injected current: see Fig. 4(a). Further simulations [8] have shown that a proper choice of the field coupling parameter within the DFB MO part of the device makes it less sensitive to the optical feedback, leading

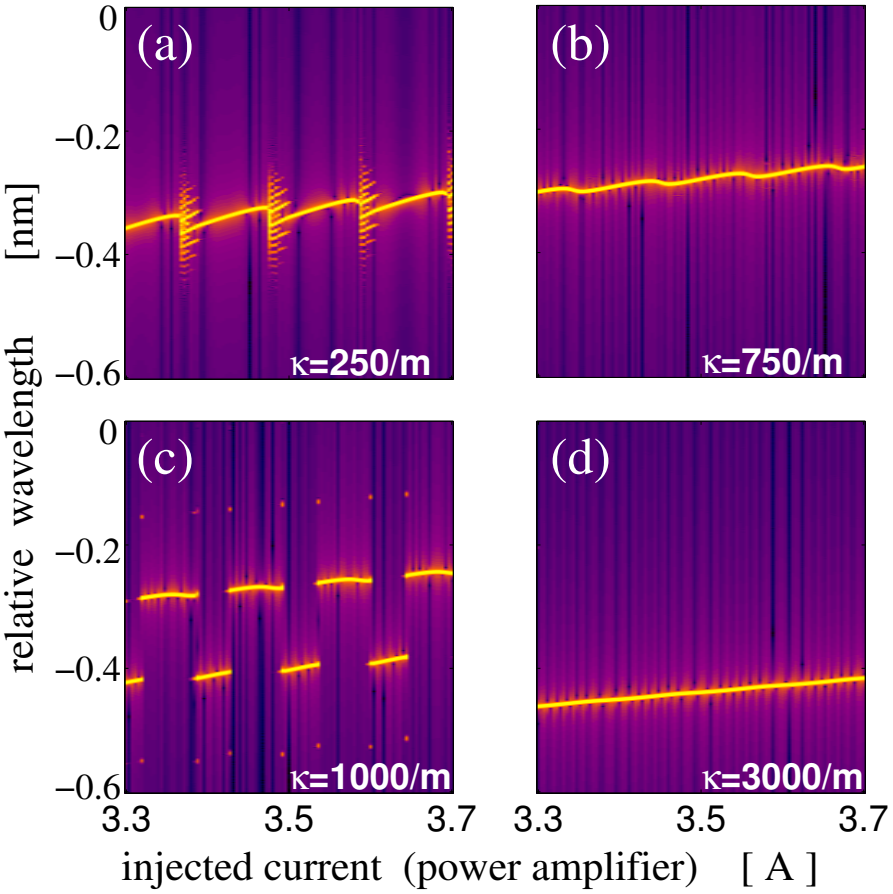

FIGURE 4. Simulated optical spectra of DFB MOPA devices with different DFB field coupling coefficients κ for an increased injected current. Each panel represents more than three days of calculations on the computer cluster using 32 processes, $(N_z \times N_x) = (800 \times 400)$ spatial mesh, and $N_t \sim 2 \cdot 10^7$ time steps.

to a stabilization of the laser emission: see panels (b) and (d) of Fig. 4. In contrast, panel (c) of the same figure shows periodically reappearing jumps between two steady states determined by the distinct resonances of the DFB MO part of the semiconductor device.

The simulation results shown in Fig. 5 represent an impact of the thermal lensing on the quality of the beam in the BAS laser. In this example, we assume a Lorentzian profile of the thermal lensing term, $c_\theta \theta(x) = \frac{2\pi}{\lambda_0} \frac{20 \cdot 10^{-12}}{x^2 + 5 \cdot 10^{-9}}$, which is similar to those considered in Refs. [12, 25]. This thermal lens profile together with the contribution of the static detuning δ is shown by the black curve in panel (a) of Fig. 5. The red dashed curve in the same figure represents the same detuning in the absence of thermal lensing. Panels (b) and (c) of the same figure represent the longitudinally averaged contribution of the electronic detuning, $\tilde{n}(N)$, and the sum of all these contributions, respectively. The time-averaged far-fields (radiation angles) and the near-fields (emission intensities directly at the laser facet) shown in panels (d) and (e) of the same figure represent the effect of the thermal lensing on the shape of the optical fields. Whereas the width of the near-fields in both cases remains similar [panel (e)], one can clearly see the

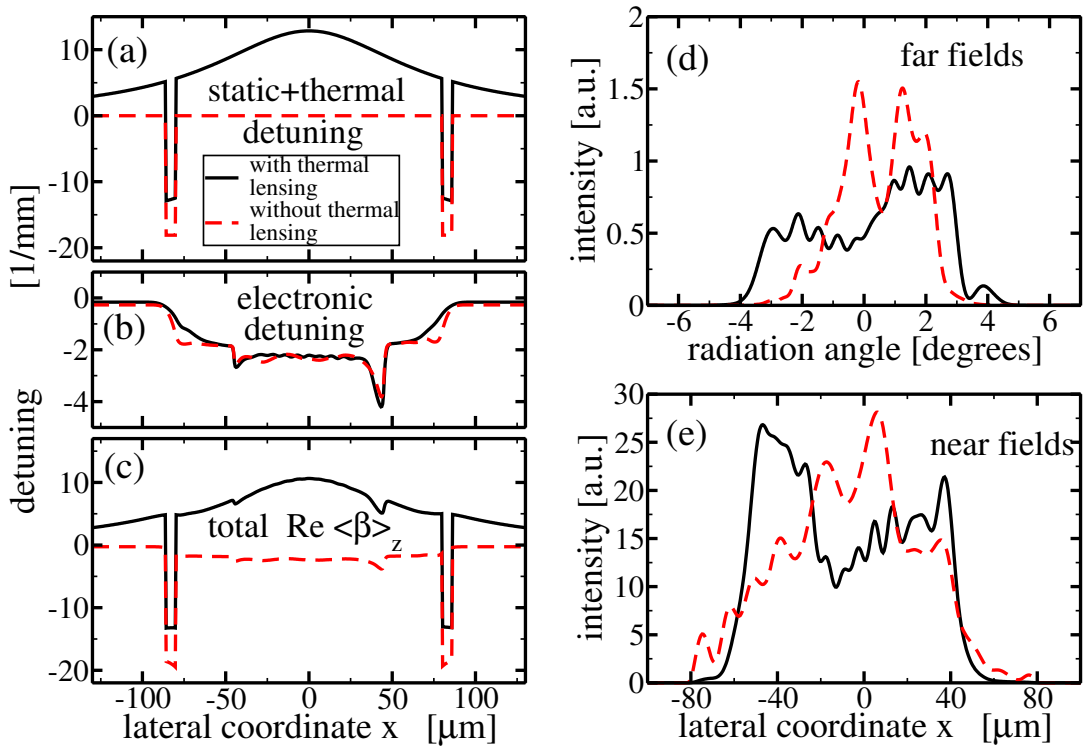

FIGURE 5. Simulated thermal lensing effects in the high-power BAS laser. Lateral distributions of the static and thermal detuning contributions $\delta + c_\theta \theta(x)$ (a), of the longitudinal averages of $\Re\beta(N)$ (b), and of the carrier-induced refractive index change $\tilde{n}(N)$ (c). (d) and (f): time-averages of the far- and near- fields. Black solid and red dashed curves represent models with and without thermal detuning term, respectively. One hour simulations on the MC computer using 25 processes, $N_t \sim 10^5$, and $(N_z \times N_x) = (800 \times 1000)$.

thermal lensing induced broadening of the radiation angles in panel (d). These undesired far-field broadening effects become even more pronounced in BAS lasers with a larger lateral size. Thus, a proper modeling and simulations of thermal effects by combining the TW and the heat transport models are strongly desired.

6. CONCLUSIONS

In conclusion, we have presented several modifications of the (2+1)-dimensional Traveling Wave model used to describe the nonlinear dynamics of broad-area edge-emitting semiconductor lasers and discussed implementation and performance of the MPI-based parallel numerical algorithms on several computers at the Weierstrass Institute in Berlin. We have found, that for typical practical problems, the optimal performance of simulations can be achieved when using $25 - 30$ processes providing a speedup factor of $20 - 25$ and calculation efficiency of $0.7 - 0.8$. For faster simulations of the problems defined on *longer* domains with a larger longitudinal mesh size N_z, one can utilize several available multi-core computers, attributing not more than one process to each available core. Finally, we have accounted for different thermal effects and presented an example of practical optimization simulations of the Master

Oscillator Power Amplifier semiconductor laser. Here, 32-process parallel computations of a single numerical one-parameter continuation diagram on the blade cluster took more than three days. Besides of practical importance, these results confirm the necessity of the parallelization of the numerical algorithm for an adequate study of laser parameters in a reasonable time. It is noteworthy that long simulation time will become a critical issue when considering the combined TW and heat transport model. Thus, we should also find a way to improve the scalability of the parallel numerical algorithm executed by hundred and even several hundreds of processes. Due to the moderate number of discretization points in the longitudinal direction (typically $N_z \leq 2000$), we should implement a possibility of the domain decomposition in both, longitudinal and lateral, directions.

REFERENCES

[1] Chazan P, Mayor J, Morgott S et al. High-power near difraction-limited tapered amplifiers at 1064 nm for optical intersatelite communications. *IEEE Phot. Techn. Lett.* 1998; 10(11): 1542–1544.

[2] Schultz W and Poprawe R. Manufacturing with nover high-power diode lasers. *IEEE J. Sel. Top. Quantum Electron.* 2000; 6(4): 696–705.

[3] Pessa M, Näppi J, Savolainen P et al. State-of-the-art aluminum-free 980-nm laser diodes. *J. Ligthw. Technol.* 1996; 14(10): 2356–2361.

[4] Maiwald M, Schwertfeger S, Güther R et al. 600 mW optical output power at 488 nm by use of a high-power hybrid laser diode system and a periodically poled MgO:$LiNbO_3$. *Optics Lett.* 2006; 31(6): 802–804.

[5] Burkhard T, Ziegler M, Fischer I et al. Spatio-temporal dynamics of broad area semiconductor lasers and its characterization. *Chaos Solitons Fractals* 1999; 10: 845–850.

[6] Tijero J, Borruel L, Vilera M et al. Simulation and geometrical design of multi-section tapered semiconductor optical amplifiers at 1.57 μm. In *Semiconductor Lasers and Laser Dynamics VI*, *Proc. SPIE*, volume 9134. p. 91342A.

[7] Spreemann M, Lichtner M, Radziunas M et al. Measurement and simulation of distributed-feedback tapered master-oscillators power-amplifiers. *IEEE J. of Quantum Electron.* 2009; 45: 609–616.

[8] Tronciu V, Lichtner M, Radziunas M et al. Improving the stability of distributed-feedback tapered master-oscillator power-amplifiers. *Opt. and Quantum Electron.* 2009; 41: 531–537.

[9] Böhringer K and Hess O. A full-time-domain approach to spatio-temporal dynamics of semiconductor lasers. I. Theoretical formulation. *Progress in Quantum Electronics* 2008; 32(5-6): 159–246.

[10] Lim J, Sujecki S, Lang L et al. Design and simulation of next-generation high-power, high-brightness laser diodes. *IEEE J. Sel. Top. Quantum Electron.* 2009; 15(3): 993–1008.

[11] Perez-Serrano A, Javaloyes J and Balle S. Spectral delay algebraic equation approach to broad area laser diodes. *IEEE J. Sel. Top. Quantum Electron.* 2013; 19(5): 1502808.

[12] Wenzel H. Basic aspects of high-power semiconductor laser simulation. *IEEE J. Sel. Top. Quantum Electron.* 2013; 19(5): 1–13.

[13] Radziunas M, Tronciu V, Bandelow U et al. Mode transitions in distributed-feedback tapered master-oscillator power-amplifier. *Opt. and Quantum Electron.* 2008; 40: 1103–1109.

[14] Radziunas M, Herrero R, Botey M et al. Far field narrowing in spatially modulated broad area edge-emitting semiconductor amplifiers. *J. Opt. Soc. Am. B* 2015; 32: 993–1000.

[15] Pimenov A, Tronciu V, Bandelow U et al. Dynamical regimes of a multistripe laser array with external off-axis feedback. *J. Opt. Soc. Am. B* 2013; 30: 1606.

[16] Čiegis R, Radziunas M and Lichtner M. Numerical algorithms for simulation of multisection lasers by using traveling wave model. *Math. Model. Anal.* 2008; 13: 327–348.

[17] Čiegis R and Radziunas M. Effective numerical integration of traveling wave model for edge-emitting broad-area semiconductor lasers and amplifiers. *Math. Model. Anal.* 2010; 15: 409–430.

[18] Radziunas M and Čiegis R. Effective numerical algorithm for simulations of beam stabilization in broad area semiconductor lasers and amplifiers. *Math. Model. Anal.* 2014; 19: 627–646.

[19] BALaser: a software tool for simulation of dynamics in broad area semiconductor lasers. http://www.wias-berlin.de/software/balaser/.

[20] Radziunas M. Modeling and simulations of edge-emitting broad-area semiconductor lasers and amplifiers. In Wyrzykowski R, Deelman E, Dongarra J et al. (eds.) *Parallel Processing and Applied Mathematics: 11th International Conference, PPAM 2015, Krakow, Poland, September 6-9, 2015. Revised Selected Papers, Part II*, *Lecture Notes in Computer Science*, volume 9574. Springer, 2016. pp. 269–276.

[21] Bandelow U, Radziunas M, Sieber J et al. Impact of gain dispersion on the spatio-temporal dynamics of multisection lasers. *IEEE J. of Quantum Electron.* 2001; 37: 183–188.

[22] Jechow A, Lichtner M, Menzel R et al. Stripe-array diode-laser in an off-axis external cavity: Theory and experiment. *Optics Express* 2009; 17: 19599–19604.

[23] Zink C, Jechow A, Heuer A et al. Multi-wavelength operation of a single broad area diode laser by spectral beam combining. *IEEE Phot. Techn. Letters* 2014; 26(3): 253–256.

[24] Bandelow U, Gajewski H and Hünlich R. Fabry-Perot lasers: thermodynamics-based modeling. In Piprek J (ed.) *Optoelectronic Devices - Advanced Simulation and Analysis*, chapter 5. New York: Springer, 2005. pp. 63–85.

[25] Bawamia A, Eppich B, Paschke K et al. Experimental determination of the thermal lens parameters in a broad area semiconductor laser amplifier. *Applied Physics B* 2009; 97: 95–101.